Journal of Nuclear Materials 398 (2010) 172–179

Contents lists available at ScienceDirect

Journal of Nuclear Materials

journal homepage: www.elsevier.com/locate/jnucmat

Analysis of corrosion scale structure of pre-oxidized stainless steel 316 in molten lead bismuth eutectic and the relation to impedance spectroscopy response

Xiang Chen [a], James F. Stubbins [a,*], Peter Hosemann [b], Alan Michael Bolind [a]

[a] Department of Nuclear, Plasma, and Radiological Engineering, University of Illinois at Urbana-Champaign, 104 South Wright Street, Urbana, IL 61801, USA
[b] Los Alamos National Laboratory, P.O. Box 1663, Los Alamos, NM 87545, USA

A B S T R A C T

Stainless steel 316 is a candidate structural material for heavy liquid metal spallation neutron sources and fast reactor systems. Impedance spectroscopy (IS) provides a means of real-time measurements of the stability of protective oxide scales in these systems. The IS technique has been shown to yield quantitative results at lower temperatures, but does not yet yield quantitative results at temperatures of interest for engineering applications. To understand this, pre-oxidized stainless steel 316 samples were immersed in oxygen-saturated stagnant lead bismuth eutectic at 550 °C for 1335 h. During the exposure, real-time impedance spectroscopy was taken from different samples. Negligible impedance was observed from one sample at the end of 1335 h, indicating that the oxide scale was non-protective. A variety of microanalysis techniques revealed that oxide layers formed on the sample surface suffered corrosion attack from the LBE. A duplex oxide structure composed of outer iron oxide and inner iron chromium oxide was found on some sample surface area. The major phases of the duplex oxide scales were Fe_3O_4 and $FeCr_2O_4$. The high conductivity of this duplex scale explains the corrosion rate as well as the lack of IS response.

1. Introduction

Lead and Lead–Bismuth Eutectic (LBE) have been proposed as candidate coolant materials for the next generation nuclear reactors. They can also be used as both coolants and neutron spallation sources in the Accelerator Driven Systems (ADS) because of their favorable physical and chemical properties for these applications, such as low melting point, low reactivity, low vapor pressure, low viscosity, good gamma shielding, and high neutron yield [1,2]. However, LBE at high temperature is very corrosive towards Stainless Steel 316 (SS316) which is widely used as structure materials in nuclear systems. An extensive amount of work on the corrosion behavior of SS316 in LBE by many researchers has been reported [3–12]. The results from those studies indicate that the main reason for the corrosion of SS316 in LBE is that major alloying components of SS316, especially Ni, have high solubility in high temperature LBE. To address this, various methods for mitigating the corrosion attack of LBE have been proposed; the most prevalent one is Active Oxygen Control (AOC) of LBE. The concept behind AOC is to maintain a low level of oxygen in the liquid LBE to facilitate the formation of protective oxide layers on the steel surface. Once the oxide layers are formed, a direct contact between the steel and LBE would be eliminated and any of the active alloying components in the steel would have to diffuse through the oxide layer to reach the LBE. Hence it is suggested that AOC can be used to enhance the corrosion resistance of SS316 in LBE.

In order to ensure that protective corrosion scales form during LBE exposure, impedance spectroscopy (IS) is being developed as a means of characterize the corrosion process in real-time. Previously, Lillard et al. also applied IS technique to measure the impedance response from SS316 in LBE [13]. Other IS results have been reported by Stubbins et al. [14]. These studies have concentrated on lower temperatures where quantifiable impedance response can be seen and the progression of scale development during corrosion can be monitored. The main interest, however, is to develop this technique for higher temperature applications which are of more direct interest to real reactor or accelerator conditions. During experiments to monitor IS response at higher temperature, typically no change in impedance response can be measured. This indicates both that it is difficult to apply IS technology at temperatures of interest, and that the oxide scales which are intended to be protective are highly conductive instead. The conductivity is related to the ionic species conduction that supports corrosion. The principle for the application of IS is that, if significant impedance is measured, then oxide layers must be present on SS316 surface which would induce a resistant layer between the conductive properties of SS316 and the LBE. If the layer has high impedance

* Corresponding author. Tel.: +1 217 333 6474; fax: +1 217 333 2906.
E-mail address: jstubbin@illinois.edu (J.F. Stubbins).

0022-3115/$ - see front matter © 2010 Elsevier B.V. All rights reserved.
doi:10.1016/j.jnucmat.2009.10.029

Table 1
Composition for SS316.

Elements(wt.%)	Fe	C	P	S	Cr	Ni	Mo	Mn	Si
SS316	Bal.	0.03–0.08	0.045	0.03	16.0–18.0	10.0–14.0	2.0–3.0	2.0	1.0

Fig. 1. Final assembly of one sample coupon.

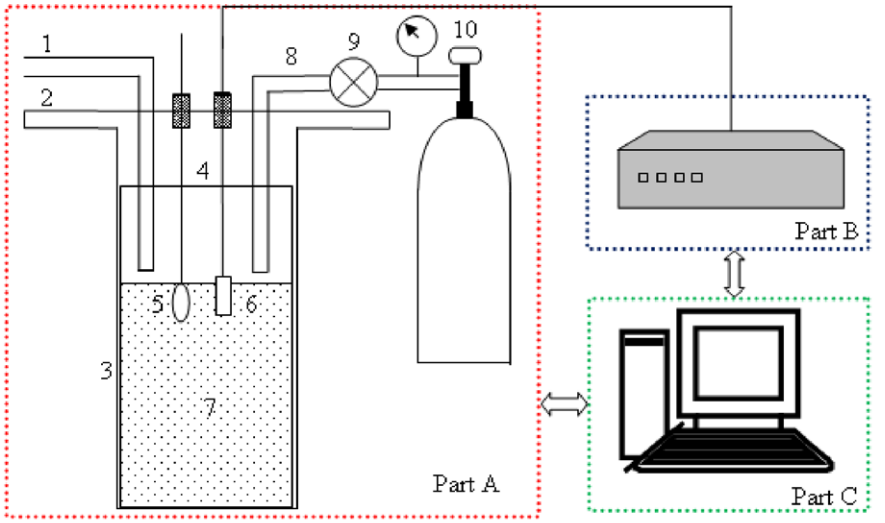

Part A—corrosion test setup, 1—gas outlet, 2—top lid, 3—stainless steel heating pot, 4—quartz crucible, 5—thermal couple, 6—SS316 sample, 7—LBE, 8—gas inlet, 9—gas flow meter, 10—argon gas tank, Part B—impedance measurement system, Part C—computer controller

Fig. 2. Layout of the corrosion test facilites.

it is presumed to protect the steel from the corrosion; but if negligible impedance is measured, then oxide layers may not be present and/or LBE can penetrate the oxide layers [14]. The growth rate and magnitude of the measured impedance can indicate the corrosion kinetics of SS316 in high temperature LBE.

This study was conducted to understand the conductivity processes which limit IS at higher temperatures. While a number of earlier studies have been performed to understand the corrosion processes over a range of conditions, this study is intended to use a wide variety of experimental techniques to explain the features of the scale which promote high conductivity or poor impedance response.

2. Experiment

2.1. Material

SS316 plate samples were obtained from McMaster-Carr Supply Company; Table 1 shows the given composition. The plate samples were then cut into small strips with the size: 70 mm × 6.35 mm × 0.76 mm and further polished successively with 240, 320, 400, and 600 grit polishing paper. After the final polishing process, the samples were cleaned in an ultrasonic cleanser with acetone, ethanol, and deionized water in sequence. They were then pre-oxidized at 800 °C for 60 h in a horizontal tube furnace with air flow which bubbled through water before entering the tube to add water vapor. After pre-oxidation the thickness of the oxide layer on the sample surface was no more than 1 μm. Then an electrical wire was spot welded to one end of each sample strip and threaded through an insulating ceramic tube. The final assembly for each sample is illustrated in Fig. 1.

2.2. Experiment procedures

The assemblies of pre-oxidized SS316 samples were installed into the corrosion test facilities as illustrated in Fig. 2. To reduce the time needed for the initial oxide formation, SS316 samples were pre-oxidized in the moist air for a short period of time. Part A was mainly used for the static corrosion test of pre-oxidized SS316 in LBE. It had a stainless steel heating pot with a cylindrical

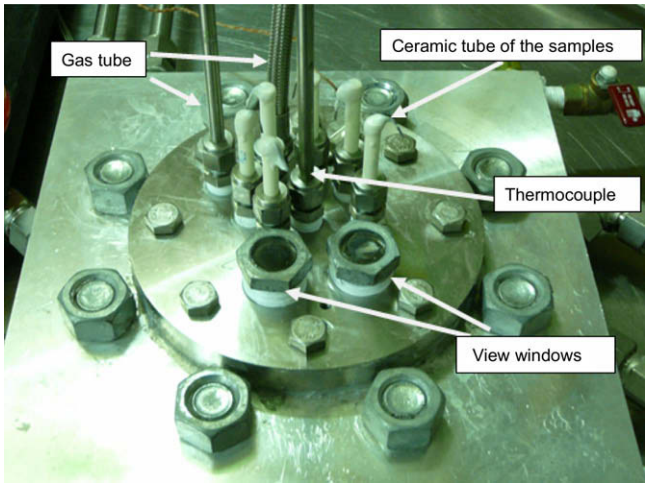

Fig. 3. Top view of the heating pot.

Table 2
Summary of corrosion experiment conditions.

Materials	Temperature	Oxygen concentration	Duration	Test environment
Pre-oxidized SS316	550 °C	1.17×10^{-3} wt.%	1335 h	Static LBE

quartz crucible in it as the container for liquid LBE. The top lid sealed the pot from the outside air and had several threaded holes in it to provide access for samples, gas pipes, thermocouples and view windows as shown in Fig. 3. Swagelok tube fittings were used in connection sites to provide a good seal. A gas inlet connected to an argon gas tank coupled with a gas outlet connected to an oil bubbler was used to control the cover gas in the pot. During the experiment samples were immersed in liquid LBE with a thermocouple immersed approximately at the same depth as samples to monitor the experiment temperature. Part B indicates the hardware needed for making impedance measurement. They were consisting of a 273A potentiostat and a 5210EC dual-phase analog lock-in amplifier, both from AMETEK Princeton Applied Research. Part C shows the computer used to control and monitor both part A and part B. A LabVIEW program was used to control the LBE temperature and cover gas flow rate and also keep records of experiment parameters, such as temperature, time, gas pressure, etc. Another program called PowerSINE developed by AMETEK Princeton Applied Research was the software used to make impedance measurements on pre-oxidized SS316 samples. At first, the liquid LBE was heated to 200 °C and the samples were immersed approximately half of their length into the liquid LBE. In order to increase the temperature of LBE into the target temperature which was 550 °C in this study, an inert gas environment was needed to avoid excess LBE oxidation. Hence argon cover gas was used to flush the pot via the gas inlet at a gas flow rate of 0.25 standard liters per minute (at 1 atm and 25 °C) for the initial 24 h. After that, the temperature of LBE was increased from 200 °C to 550 °C at a heating rate of 4.5 °C/min and the gas flow rate was lowered to 0.10 standard liters per min (at 1 atm and 25 °C) for the remaining time of the experiment. Even with pure argon cover gas, the oxygen content in liquid LBE was still saturated, because the oxygen partial pressure in argon exceeded the saturation partial pressure of oxygen in LBE. This can be confirmed by the formation of LBE oxide on top of liquid LBE. Because of lacking of a suitable oxygen sensor, oxygen monitoring and control were not implemented in this study. The oxygen saturation concentration was calculated to be

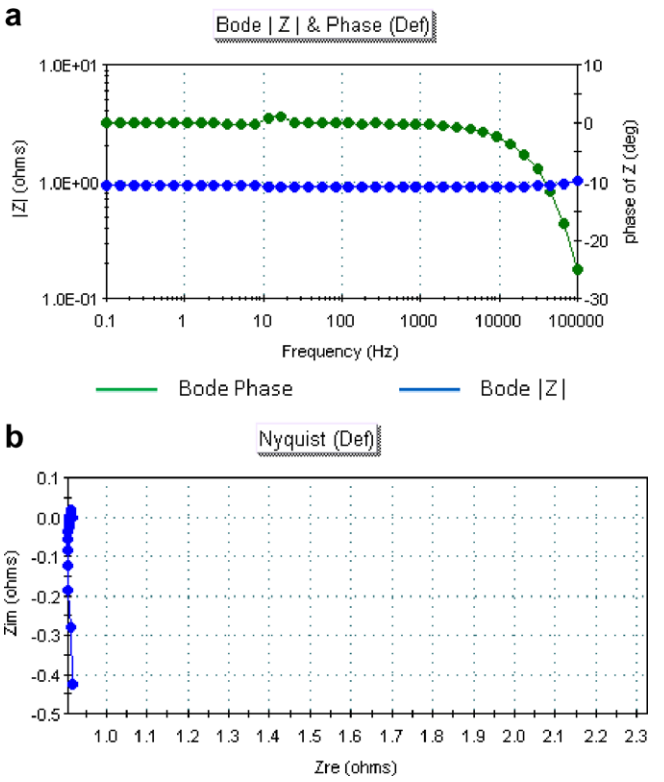

Fig. 4. IS results of the pre-oxidized SS316 sample at the end of the corrosion experiment. (a) Impedance magnitude and phase plot and (b) imaginary impedance versus real impedance at different frequencies.

1.17×10^{-3} wt.% at 550 °C [16]. Table 2 summarizes the experiment conditions. During the static corrosion test, the IS measurements were continuously performed on several SS316 samples. After immersed in 550 °C LBE for 1335 h, SS316 samples were taken out of the pot and were cut into two parts. For one part of each sample, the remaining LBE on the sample surface was not cleaned and that part was mounted directly into an epoxy resin and polished for cross-section observation. The other part was cleaned in a solution with equal parts of ethanol, acetic acid and hydrogen peroxide to remove the residual LBE.

2.3. Post-exposure analyses

The post-exposure microanalyses included scanning electron microscopy (SEM), energy-dispersive X-ray spectroscopy (EDS), glancing angle X-ray diffraction (XRD), atomic force microscopy (AFM), and magnetic force microscopy (MFM). With a small incidence angle for the X-rays, glancing angle XRD can identify phases at and near the sample surface. The phase information from the surface oxide layers is important and many literatures fail to provide this information. In addition, glancing angles were varied from 1° to 14° in the hope of obtaining information about the amount change of various phases at different depths from the surface. The principle for this application is that the larger the glancing angle is, the deeper the X-ray can penetrate. Hence different glancing angles can be applied to measure phases at different distances from the sample surface. AFM is a unique technique for imaging, measuring and even manipulating matter at the size of nanoscale. It has gained vast popularity from many research fields. However this technique has not been widely used to analyze the oxide layers formed on metals corroded in LBE. In this study by scanning across the sample surface, AFM can measure the three dimensional topography of the sample with a sharpened probe [15]. MFM is similar to

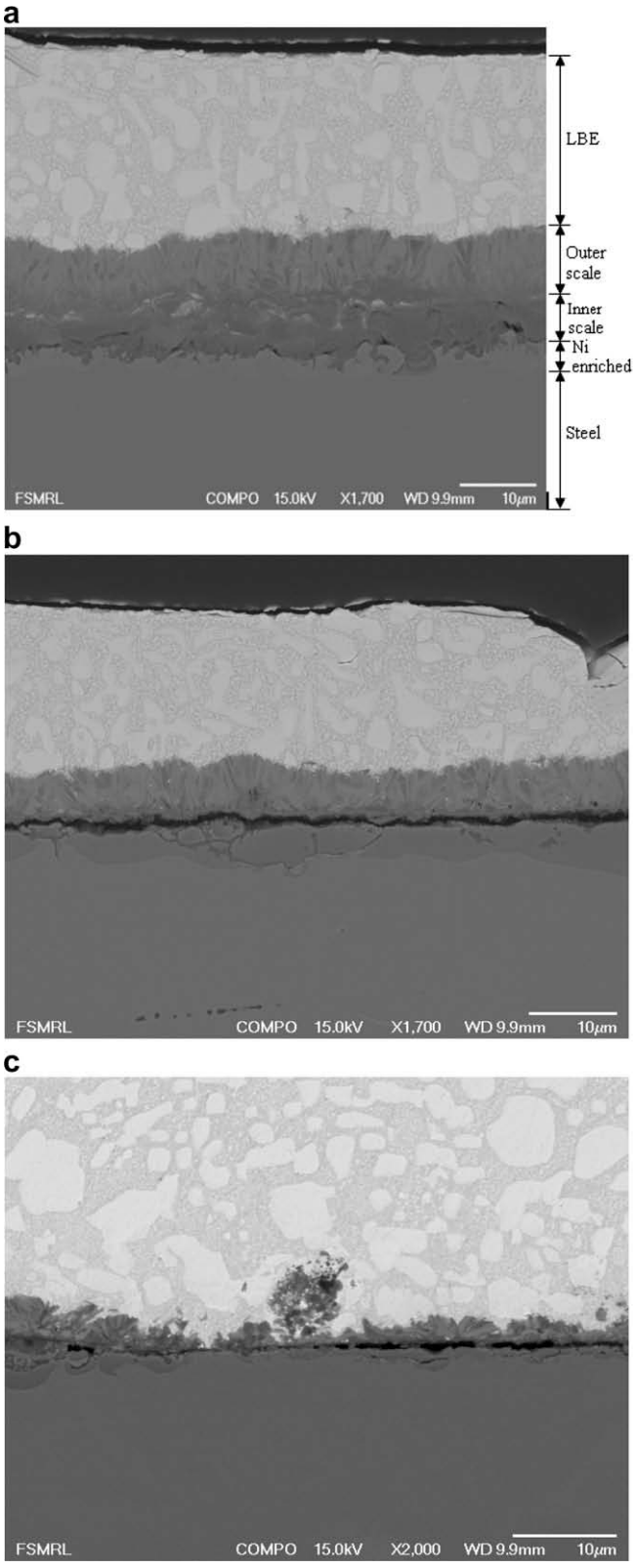

Fig. 5. Post-exposure cross-section SEM pictures of the pre-oxidized SS316 sample. (a) Duplex oxide structure, (b) cracks formed within the inner oxide layer and (c) outer oxide layer spalled off.

AFM except that a probe with magnetic coating must be used and additional magnetic field response from the scanned area can be measured. All the results presented in this paper were from the same pre-oxidized SS316 sample.

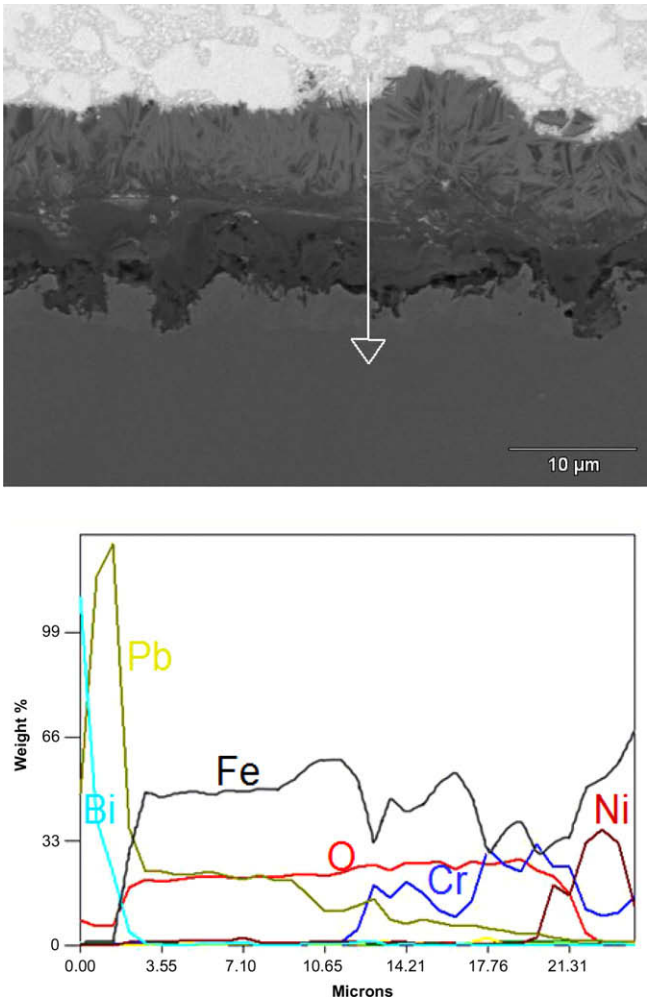

Fig. 6. EDS linescan of the duplex oxide layers.

3. Results and discussion

3.1. IS measurements

The impedance magnitude of the pre-oxidized SS316 sample was negligible at the end of the experiment. Fig. 4 shows a single impedance scan result of the sample. There was no significant real or imaginary impedance and the small measured value of impedance was from the electrical wire connecting the sample. This means that protective oxide layers which were impermeable to LBE did not form over the whole sample surface. The layer due to pre-oxidation was not maintained under these conditions.

3.2. SEM and EDS results

SEM results reveal that oxide layers formed on the sample surface were not homogeneous and their appearances varied from place to place. Fig. 5a–c illustrate several backscattering electron (BSE) images from different cross-section areas of the pre-oxidized SS316 sample. In Fig. 5a, the top bright part was the solidified LBE within which the big patches were almost pure bismuth and the regions filled with small dots were almost pure lead. Underneath the LBE existed a duplex scale which separated the SS316 alloy from the LBE. The outer layer in the scale had relatively bright column-shaped grains embedded in grey oxide matrix while the inner layer seemed more cohesive and uniform. A nickel enriched zone also existed below the inner oxide layer based on the EDS results.

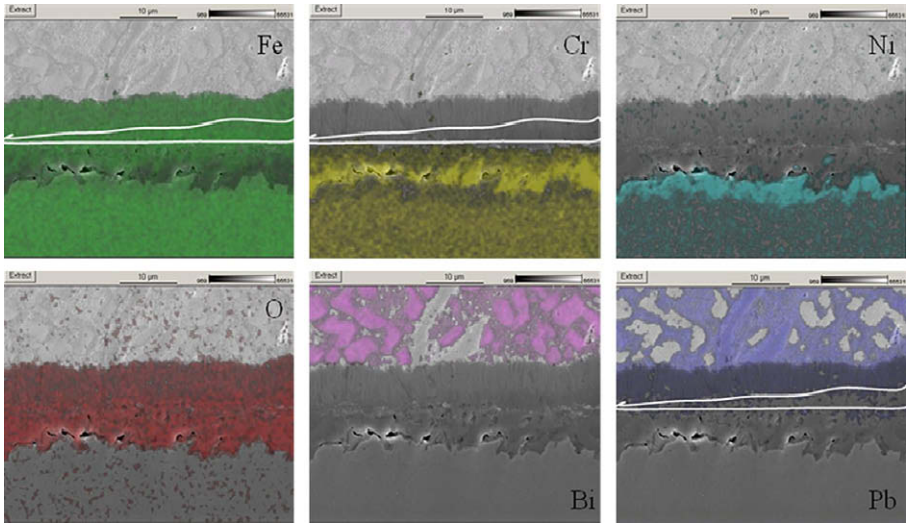

Fig. 7. EDS mapping of the duplex oxide layers.

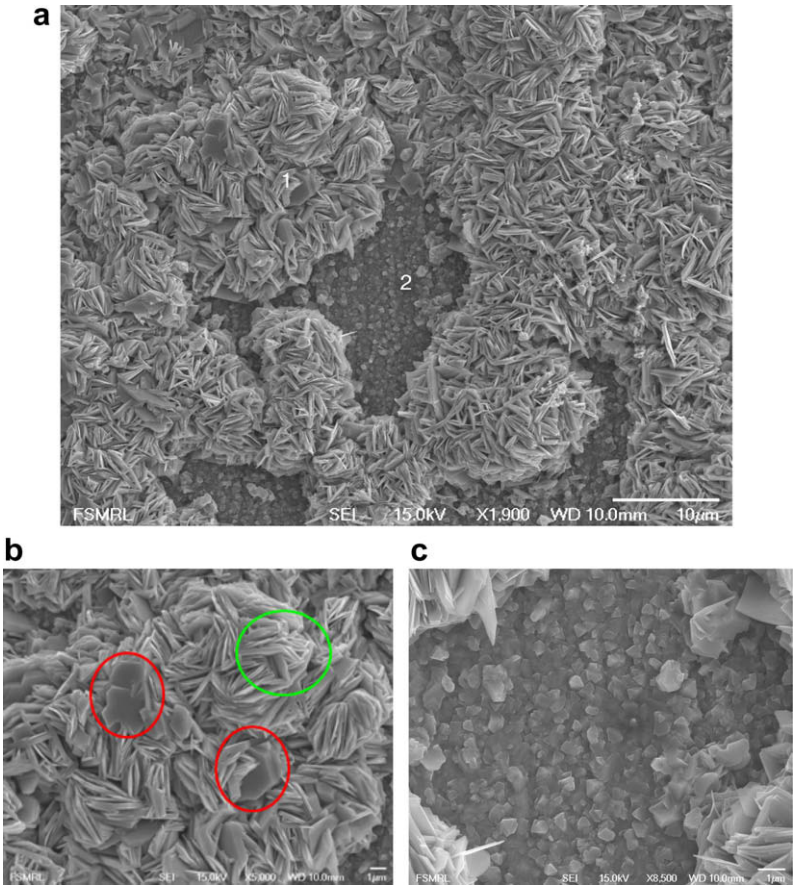

Fig. 8. (a) Post-exposure surface SEM pictures of the pre-oxidized SS316 sample; (b) magnified figure of part 1 in (a); (c) magnified figure of part 2 in (a).

There were several small bright patches between the outer layer and the inner layer of the scale. Since in the BSE image the region with higher atomic number compositions appears brighter, it is suggested that the white patch was lead compared with the color of top LBE part in Fig. 5a. Therefore, the outer oxide layer could not prevent lead penetration while the inner oxide layer was more cohesive and lead could only partially infiltrate it as confirmed by visual inspection. The average thicknesses for the outer, inner and nickel enriched zone are: 8.20 μm, 7.83 μm, and 2.72 μm based on six measurements at different cross-section areas on the sample surface. The intact duplex oxide structure could not form contiguously over the entire sample surface. Fig. 5b shows cracks which form within the inner oxide layer and Fig. 5c indicates that the outer oxide layer can spall off the sample surface. These observations also explain why negligible impedance magnitude was measured from the sample. The direct contact between

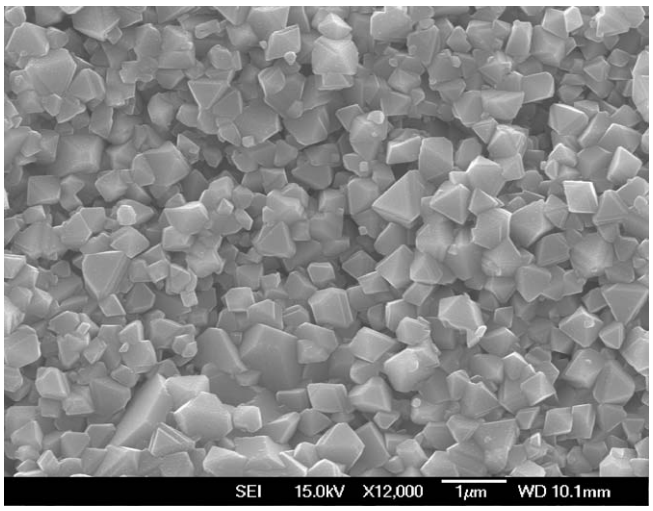

Fig. 9. Surface SEM of the pre-oxidized SS316 sample.

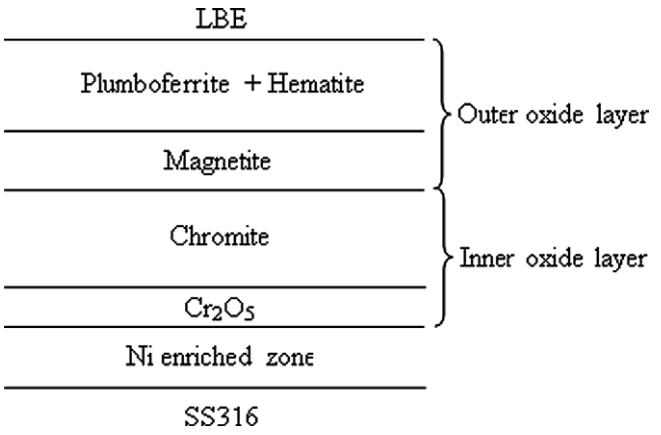

Fig. 11. Oxide layer configuration of the pre-oxidized SS316 sample after exposure.

the SS316 and LBE prohibits the possibility of obtaining a large IS response. In fact, this result is useful since it indicates the lack of protective scale formation and shows that it can be monitored in real-time at temperature.

To better understand the alloying elements distribution within the duplex oxide layers, both EDS linescan and mapping were performed on approximately the same region as shown in Fig. 5a. For instance, Fig. 6 shows an EDS quantitative linescan on typical duplex oxide layers with standards for each element except lead and bismuth. Fig. 6 shows that the outer oxide layer was mainly composed of iron oxide while the inner oxide layer had both iron and chromium. With increasing distance from the surface, the concentration of iron decreased while the concentration of chromium increased in the inner oxide layer. Based on the weight ratio between iron, chromium and oxygen, the most possible oxide forms from the sample surface to the metal-oxide interface is: Fe_2O_3, Fe_3O_4, and $FeCr_2O_4$. Nickel was enriched at the interface between the inner oxide layer and underlying steel matrix. The experimental results match well with the findings of Gnecco et al. [17] whose experiments were performed under the same condition as the current study. Many researchers believe that the outer iron oxide is Fe_3O_4 (magnetite) and the inner iron chromium oxide is basically $Fe_{II}(Fe,Cr)_2^{III}O_4$ (spinel). However, since the amount of iron and chromium changed within both outer and inner oxide layer, it is suggested that the actual oxide phases could be more complicated.

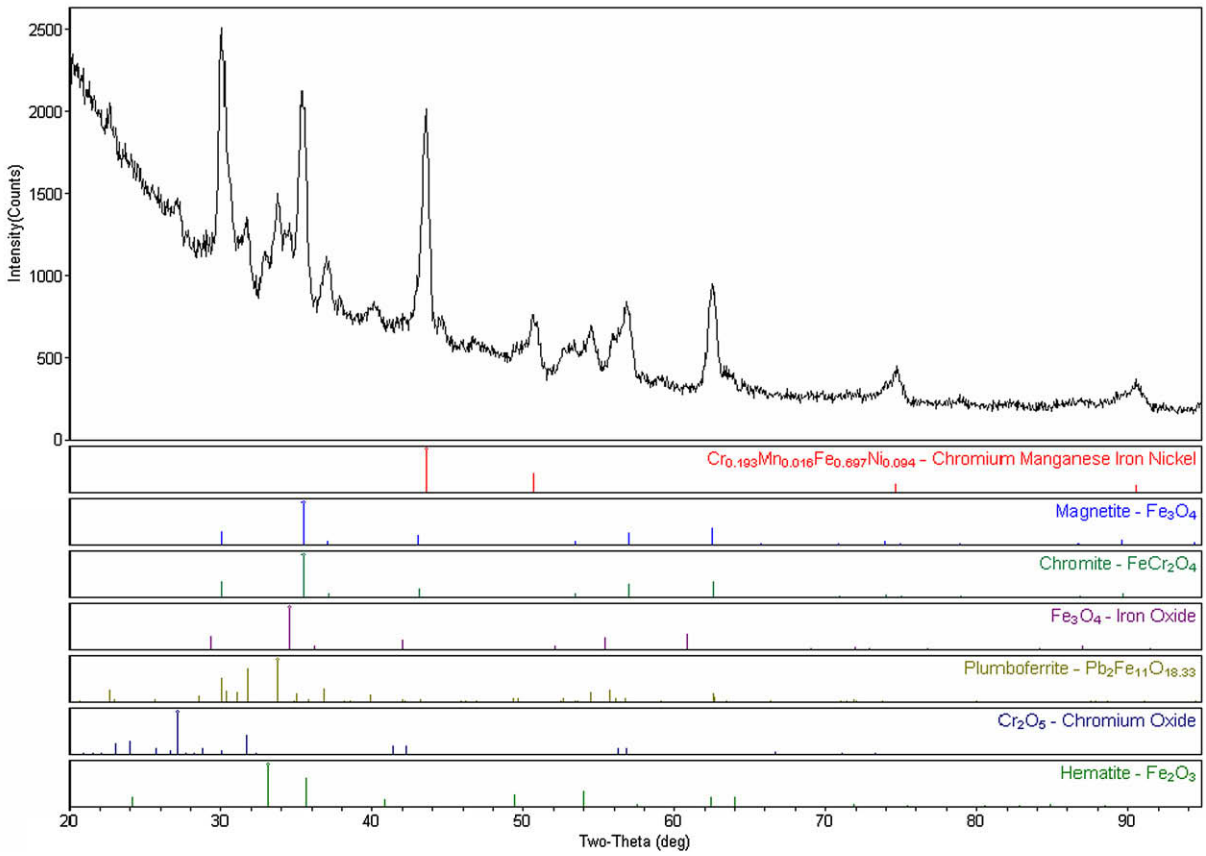

Fig. 10. Phase analysis of the pre-oxidized SS316 sample after immersion in LBE.

Hosemann et al. [2] found that the duplex oxide layers formed on the D9 stainless steel after immersion in liquid LBE at 550 °C for up to 3000 h actually had four sublayers. As for the nickel enrichment between the inner oxide layer and steel matrix, Zhang et al. [18] believed that since there was not much nickel in the oxide, nickel should diffuse into the steel during the oxide formation considering the mass balance. The other explanation for the nickel enrichment is that iron and chromium was preferentially oxidized and nickel was left behind [19]. Another important phenomenon shown in Fig. 6 is the lead penetration into the outer oxide layer. The EDS mapping of major elements of SS316 and LBE from the same cross-section area are shown in Fig. 7. To better correlate the distributions of different elements to the spatial image features, the EDS mapping was overlaid on the SEM images. The color spot on the image illustrates where the relevant element was identified and the spot density is also proportional to the concentration of the element. The results from Fig. 7 are similar to the EDS line-scan results. In the lower part of the outer iron oxide layer as highlighted by the white line, there was no significant amount of lead present. However in the upper part of the outer iron oxide layer where the relative bright column-shaped oxide grains existed, lead was present in significant amount. The difference in the ability to stop lead penetration within the outer oxide layer may indicate there are two different oxide phases for the outer oxide layer. Compared with iron and chromium, nickel dissolved slightly into the LBE which can be attributed to high solubility of nickel in LBE.

Fig. 8a–c illustrate surface morphology on the same SS316 sample. The region marked with 1 in Fig. 8a contained lead, iron, and oxygen elements and the region marked with 2 contained iron, chromium, nickel, silicon, and oxygen elements in the EDS results. Fig. 8b and c is magnified pictures of regions 1 and 2 in Fig. 8a, respectively. Based on the compositions of region 1 and 2 and their relative positions to each other it is suggested that region 1 was the outer oxide layer and the region 2 was the inner oxide layer as in Fig. 8a. In Fig. 8b there are two different crystal appearances highlighted with green and red circles. The crystal inside the green circle looks like the thin and tabular plate and is very similar to the appearance of hematite (Fe_2O_3) [20]. The crystal inside the red circle looks like a bulk patch. The magnified surface image of inner oxide layer as shown in Fig. 8c also resembles the surface oxide formed on the pre-oxidized SS316 sample as shown in Fig. 9. The granular crystal habit is a sign of the Fe_3O_4 and $FeCr_2O_4$.

3.3. XRD results

Glancing angle XRD phase analysis reveals that major phases in the duplex oxide layers were Fe_3O_4 (magnetite) and $FeCr_2O_4$ (chromite) as shown in Fig. 10. Besides those, minor oxide phases, such as $Pb_2Fe_{11}O_{18.33}$ (plumboferrite), Cr_2O_5, and Fe_2O_3 (hematite), were also detected. Since the thickness of the oxide varied along the sample surface, at some places the oxide was so thin that X-ray could penetrate it and reach the underlying steel which rendered the steel phase signal as shown in Fig. 10. Because of overlapping diffraction peaks of magnetite and chromite, it is impossible to determine the relative amount of these two phases at different depths from the sample surface. However the XRD results are meaningful and consistent with the SEM and EDS observations. By combining the XRD results with the SEM and EDS results, the most plausible oxide layer configuration is illustrated in Fig. 11. This configuration is consistent with the structure of oxide layers formed on iron–chromium–nickel alloys in air [19].

3.4. AFM and MFM results

Fig. 12a–b illustrates AFM and MFM images of the same cross-section area of the SS316 sample. In Fig. 12a, similar duplex oxide

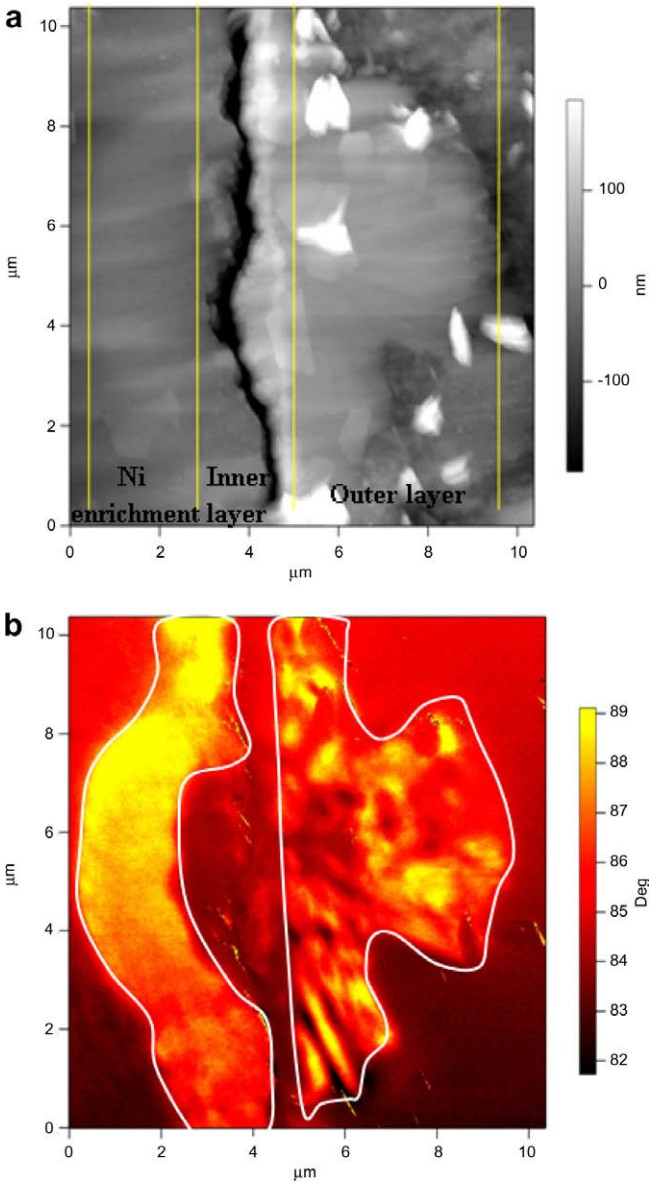

Fig. 12. (a) AFM image of the duplex oxide layers; (b) corresponding MFM image of the duplex oxide layers.

layers were found. In the corresponding MFM image Fig. 12b, the bright part highlighted with white lines showed where magnetic fields were detected. The dark part between the two bright parts was the area where no magnetic fields were detected. This means that there were magnetic fields in the outer oxide layer and nickel enriched zone while there were no magnetic fields in the inner oxide layer. As illustrated in Fig. 11, the outer oxide layer contained plumboferrite, Fe_2O_3, and Fe_3O_4, all of which are magnetic materials at the test temperature [21,22]. Nickel is also a ferromagnetic material. Therefore the outer oxide layer and nickel concentrated region showed a strong magnetic field response. In contrast, $FeCr_2O_4$ is a weakly magnetic material and Cr_2O_5 is paramagnetic at the test temperature [23]. Hence no magnetic fields were detected in the inner oxide layer.

4. Conclusions

In this study, corrosion processes of pre-oxidized SS316 samples in the oxygen-saturated stagnant LBE were examined at

550 °C for 1335 h. The impedance response was measured as an indication of the corrosion susceptibility. At the end of the experiment, negligible impedance magnitude was measured from one SS316 sample which indicated that protective oxide layers which are impermeable to LBE did not form continuously over the entire sample surface. Microanalyses confirmed the IS results that showed oxides formed on the sample surface were not homogeneous. Cracks existed within or between oxide layers and the oxides spalled off the sample surface at some places. The existing oxide on the sample surface had a duplex structure with an underlying nickel enriched zone. SEM, EDS, glancing angle XRD, AFM, and MFM were applied to characterize the duplex oxide layers. The results showed that the outer oxide layer was composed of plumboferrite, hematite, and magnetite while the inner oxide layer was consisting of chromite and Cr_2O_5. To a large extent, the results of this study are consistent with the results from existing literature. In addition, the application of techniques such as IS, glancing angle XRD, AFM and MFM provides more detailed and complementary information about the structure and growth kinetics of oxides formed on SS316.

Acknowledgements

This study is funded by the U.S. Department of Energy's, Office of Nuclear Energy's, Nuclear Energy Research Initiative (NERI) under the contract DE-FC07-051D14667. Some experiments were carried out at the Center for Microanalysis of Materials (CMM), University of Illinois at Urbana-Champaign, which is partially supported by the U.S. Department of Energy under grant DEFG02-91-ER45439. The authors would also like to express their appreciation to Dr. Jim Mabon, Dr. Mauro Sardela, and Dr. Scott MacLaren of CMM.

References

[1] OECD/NEA Nuclear Science Committee, Handbook on Lead–bismuth Eutectic Alloy and Lead Properties, Materials Compatibility, Thermal-hydraulics and Technologies, 2007 ed., ISBN 978-92-64-99002-9.
[2] P. Hosemann, M. Hawley, D. Koury, J.G. Swadener, J. Welch, A.L. Johnson, G. Mori, N. Li, J. Nucl. Mater. 375 (2008) 323–330.
[3] F. Barbier, G. Benamati, C. Fazio, A. Rusanov, J. Nucl. Mater. 295 (2001) 149–156.
[4] C. Fazio, G. Benamati, C. Martini, G. Palombarini, J. Nucl. Mater. 296 (2001) 243–248.
[5] Ph. Deloffre, A. Terlain, F. Barbier, J. Nucl. Mater. 301 (2002) 35–39.
[6] G. Benamati, C. Fazio, H. Piankova, A. Rusanov, J. Nucl. Mater. 301 (2002) 23–27.
[7] F.J. Martín, L. Soler, F. Hernández, D. Gómez-Briceño, J. Nucl. Mater. 335 (2004) 194–198.
[8] Ph. Deloffre, A. Terlain, J. Nucl. Mater. 335 (2004) 244–248.
[9] L. Soler, F.J. Martín, F. Hernández, D. Gómez-Briceño, J. Nucl. Mater. 335 (2004) 174–179.
[10] A. Aiello, M. Azzati, G. Benamati, A. Gessi, B. Long, G. Scaddozzo, J. Nucl. Mater. 335 (2004) 169–173.
[11] G. Müller, A. Heinzel, J. Konys, G. Schumacher, A. Weisenburger, F. Zimmermann, V. Engelko, A. Rusanov, V. Markov, J. Nucl. Mater. 335 (2004) 163–168.
[12] G. Benamati, A. Gessi, Ping-Zhu Zhang, J. Nucl. Mater. 356 (2006) 198–202.
[13] R.S. Lillard, C. Valot, R.J. Hanrahan, Corrosion 60 (2004) 1134–1143.
[14] J.F. Stubbins, A.M. Bolind, X. Chen, J. Nucl. Mater. 377 (2008) 243–252.
[15] P. West, Introduction to Atomic Force Microscopy: Theory, Practice and Applications, www.AFMUniversity.org.
[16] B.F. Gromov, Y.I. Orlov, P.N. Martynov, V.A. Gulevskiy, in: Proceedings of the Conference of the Heavy Liquid Metal Coolants in Nuclear Technology, Obninsk, Russian Federation, 1998, pp. 87–100.
[17] F. Gnecco, E. Ricci, C. Bottino, A. Passerone, J. Nucl. Mater. 335 (2004) 185–188.
[18] J. Zhang, N. Li, Y. Chen, A.E. Rusanov, J. Nucl. Mater. 336 (2005) 1–10.
[19] D. Talbot, J. Talbot, Corrosion Science and Technology, first ed., CRC Press, Boca Raton, Florida, 1998.
[20] W.M.M. Huijbregts, Elektrotechniek 49 (1971) 254–259.
[21] P. Hosemann, M. Hawley, G. Mori, N. Li, S.A. Maloy, J. Nucl. Mater. 376 (2008) 289–292.
[22] M. Tokar, J. Am. Ceram. Soc. 52 (1969) 302–306.
[23] T.A. Hewston, B.L. Chamberland, J. Magn. Magn. Mater. 43 (1984) 89–95.